A'–*B* Intersite Cooperation-Enhanced Water Splitting in Quadruple Perovskite Oxide $CaCu_3Ir_4O_{12}$

Xubin Ye,[†,§,◊] Sanzhao Song,[‡,◊] Lili Li,[‡] Yu-Chung Chang,[∥] Shijun Qin,[†,§,] Zhehong Liu,[†,§,] Yu-Cheng Huang,[⊥] Jing Zhou,[‡] Lin-juan Zhang,[‡] Chung-Li Dong,[⊥] Chih-Wen Pao,[∥] Hong-Ji Lin,[∥] Chien-Te Chen,[∥] Zhiwei Hu,[*,#] Jian-Qiang Wang,[*,‡,§] and Youwen Long[*,†,§,▽]

[†]Beijing National Laboratory for Condensed Matter Physics, Institute of Physics, Chinese Academy of Sciences, Beijing 100190, China

[‡]Key Laboratory of Interfacial Physics and Technology, Shanghai Institute of Applied Physics, Chinese Academy of Sciences, Shanghai 201800, China

[§]University of Chinese Academy of Sciences, Beijing 100049, China

[∥]National Synchrotron Radiation Research Center, 101 Hsin-Ann Road, Hsinchu 30076, Taiwan

[⊥]Department of Physics, Tamkang University, 151 Yingzhuan Rd., New Taipei City 25137, Taiwan

[#]Max Planck Institute for Chemical Physics of Solids, Nöthnitzer Straße 40, Dresden 01187, Germany

[▽]Songshan Lake Materials Laboratory, Dongguan 523808, China

Supporting Information

Supporting Tables

Table S1. Crystallographic parameters of $CaCu_3Ir_4O_{12}$ refined from XRD pattern at RT[a].

atom	site	*x*	*y*	*z*	$100\times U_{iso}$ (Å^2)	*G*
Ca	2*a*	0	0	0	1.23(2)	0.99(1)
Cu	6*b*	0	0.5	0.5	0.24(6)	0.96(1)
Ir	8*c*	0.25	0.25	0.25	0.22(1)	1.00(1)
O	24*g*	0.3060(1)	0.1699(4)	0	1.73(2)	1.07(2)

[a] Space group *Im*−3 (No. 204), a = 7.46996(1) Å, R_{wp} = 4.35%, R_p = 3.2%, χ^2=2.688, *G* represents the site occupancy factor.

Table S2. Selected bond lengths and angles for $CaCu_3Ir_4O_{12}$.

Parameters	Values
d_{Ca-O} (×12) (Å)	2.615(3)
d_{Cu-O} (×4) (Å)	1.926(3)
d_{Cu-O} (×4) (Å)	2.860(3)
d_{Ir-O} (×6) (Å)	2.005(1)
∠Ir−O−Ir (º)	137.3(2)
∠Cu−O−Ir (º)	110.7(1)
∠O−Ir−O (º)	88.8(1)
∠O−Cu−O (º)	82.4(2)

Table S3. ICP-OES analysis of dissolved Ca, Cu and Ir ions for $CaCu_3Ir_4O_{12}$ after the durability test.

Sample amount	10 μg
Concentration of Ca ion (ppb)	0.021
Concentration of Cu ion (ppb)	0.12
Concentration of Ir ion (ppb)	0.24
Loss of mass (Ca)	6.17 %
Loss of mass (C_U)	7.45 %
Loss of mass (Ir)	0.037 %

Table S4. Summary of the HER performance for $CaCu_3Ir_4O_{12}$ and other state-of-the-art perovskite electrocatalysts.

Catalyst	Electrolyte	η_{10} (mV)[a]	Tafel slope (mV·dec^{-1})	Ref.
$CaCu_3Ir_4O_{12}$	1 M KOH	187	39	This work
IrO_2	1 M KOH	291	53	This work
Pt/C	1 M KOH	65	32	This work
$Pr_{0.5}$BSCF	1 M KOH	237	45	[1]
LBSCOF	1 M KOH	180	44	[2]
SNCF-NR	1 M KOH	232	103	[3]
LBSCCF	1 M KOH	338	80	[4]
3DOM-LFC82	1 M KOH	350	110	[5]
SCFP nanofilm	1 M KOH	110	94	[6]
$SrCo_{0.7}Fe_{0.25}Mo_{0.05}O_{3-\delta}$	1 M KOH	323	94	[7]
$LaCo_{0.94}Pt_{0.06}O_{3-\delta}$	0.1 M KOH	294	148	[8]
$(Gd_{0.5}La_{0.5})BaCo_2O_{5.75}$	1 M KOH	185	28	[9]
$NdBaMn_2O_{5.5}$	1 M KOH	290	87	[10]
$PrBaCo_2O_{5.5}$	1 M KOH	245	89	[11]
Sr_2RuO_4	1 M KOH	61	51	[12]

[a] η_{10} presents overpotentials at the current density of 10 mA·cm^{-2}.

Table S5. Structural parameters of $CaCu_3Ir_4O_{12}$ and reference samples with various potentials extracted from the Ir L_3-edge EXAFS fitting.[a]

Measure conditions	Atomic scatter	No. of atoms (CN)[b]	Interatomic distance (Å)[c]	Debye-Waller factor (10^{-3}×Å^2)[d]	ΔE_0(eV)[e]	R factor
IrO_2	Ir−O	5.9±0.62	2.0186	4.6±1.4	9.8±1.6	0.008
$CaCu_3Ir_4O_{12}$	Ir−O	5.4±0.60	2.0114	2.2±1.5	9.3±1.2	0.007
OCP	Ir−O	5.5±0.66	2.0195	2.0±1.6	9.1±1.3	0.008
1.35 V	Ir−O	5.5±0.56	2.0199	2.0±1.5	9.4±1.1	0.005
1.45 V	Ir−O	5.4±0.50	2.0188	2.4±1.3	9.7±1.0	0.005
1.48 V	Ir−O	5.3±0.58	2.0150	1.9±1.4	9.7±1.2	0.006
1.50 V	Ir−O	5.3±0.70	2.0131	2.0±1.9	9.8±1.5	0.009

[a] S_0^2 was fixed as 0.79 during EXAFS fitting. [b] CN is the coordination number. [c] Interatomic distance is the bond length between Ir central atoms and surrounding coordination atoms. [d] Debye-Waller factor is a measure of thermal and static disorder in absorber-scattering distances. [e] ΔE_0 is the difference between the zero kinetic energy value of the sample and that of the theoretical model.

Table S6. Structural parameters of $CaCu_3Ir_4O_{12}$ with various time extracted from the Ir L_3-edge EXAFS fitting.

Measure conditions	Atomic scatter	No. of atoms (CN)	Interatomic distance (Å)	Debye-Waller factor (10^{-3}×Å^2)	ΔE_0(eV)	R factor
OCP	Ir-O	5.5±0.90	2.0151	2.9±2.5	8.9±1.9	0.013
1min	Ir-O	5.4±0.90	2.0103	2.6±2.4	8.5±1.9	0.014
2min	Ir-O	5.4±0.86	1.9990	2.3±2.3	8.9±1.9	0.016
4min	Ir-O	5.4±0.77	1.9971	2.7±2.0	8.8±1.7	0.012
6min	Ir-O	5.4±0.86	1.9961	2.1±2.4	8.9±1.9	0.017
8min	Ir-O	5.4±0.99	1.9861	3.0±2.5	8.6±2.1	0.019
10min	Ir-O	5.3±0.85	1.9824	2.7±2.2	9.1±1.8	0.016
15min	Ir-O	5.3±0.51	1.9740	3.3±2.6	9.4±1.1	0.019
20min	Ir-O	5.3±0.49	1.9710	3.3±2.6	9.1±1.04	0.017
25min	Ir-O	5.2±0. 90	1.9711	2.6±2.3	9.5±1.99	0.017
30min	Ir-O	5.2±0. 66	1.9706	2.5±1.8	9.7±1.50	0.009

Supporting Figures

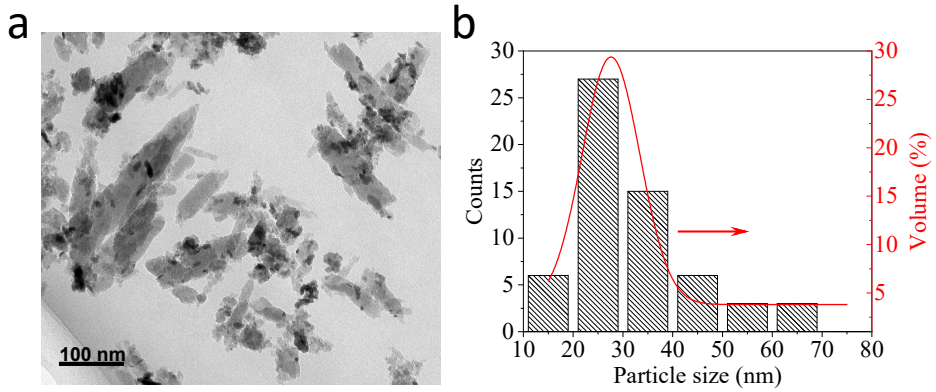

Figure S1. The particle size analysis using the TEM method. (a) The TEM image of $CaCu_3Ir_4O_{12}$. (b) Distribution histogram for the particle size of $CaCu_3Ir_4O_{12}$ catalyst derived from (a).

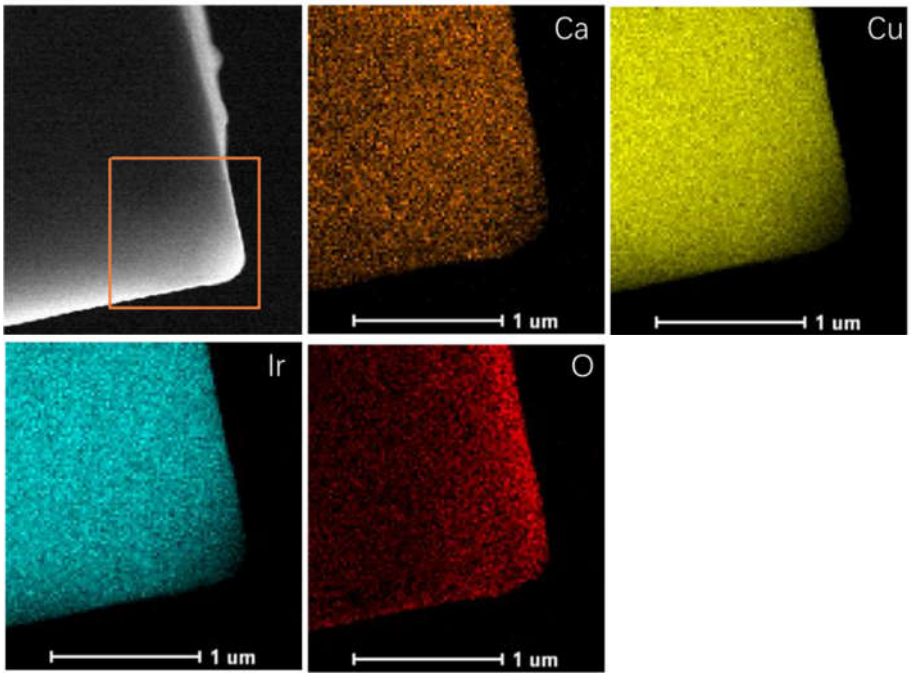

Figure S2. Elemental mapping images of $CaCu_3Ir_4O_{12}$.

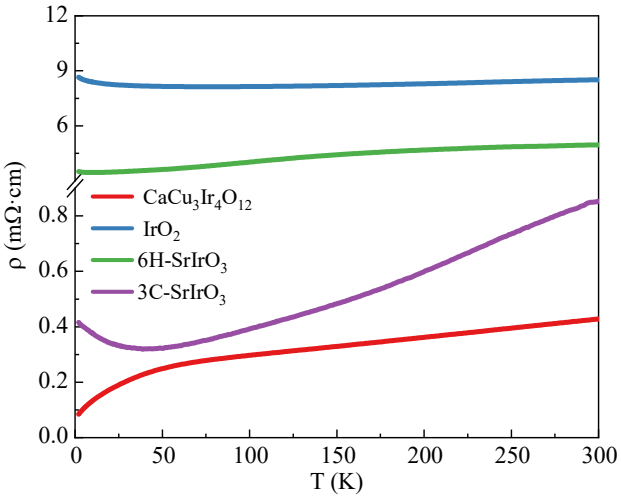

Figure S3. Temperature-dependent resistivity measured between 2–300 K for $CaCu_3Ir_4O_{12}$, 6H-$SrIrO_3$, 3C-$SrIrO_3$ and IrO_2.

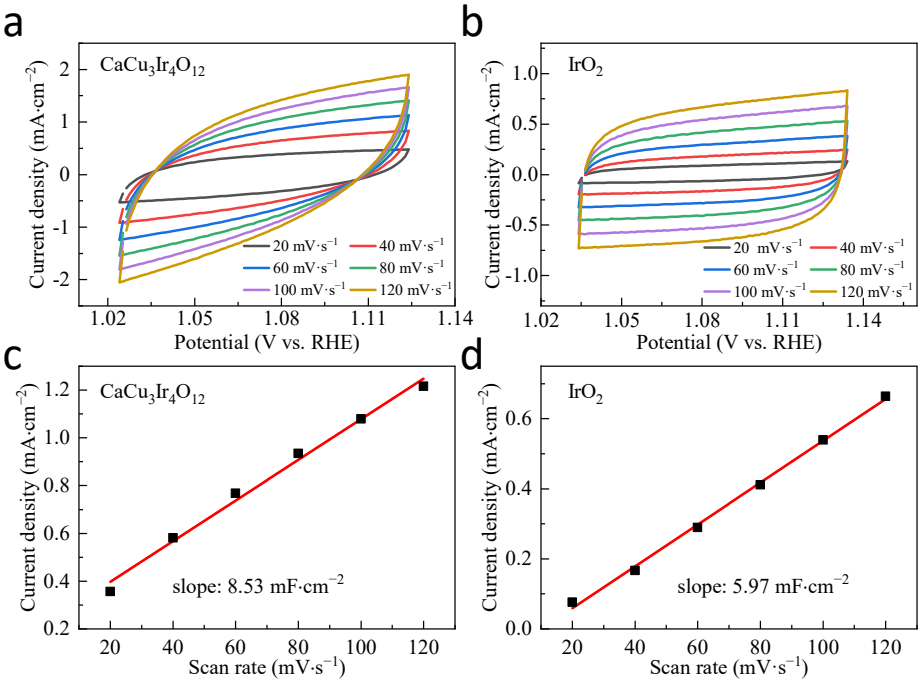

Figure S4. ECSA analyses of $CaCu_3Ir_4O_{12}$ and commercial IrO_2 catalysts. (a) and (b) Cyclic voltammograms at different scan rates in a potential window where no Faradaic processes occur (1.02 to 1.12 V vs. RHE) for $CaCu_3Ir_4O_{12}$ and IrO_2, respectively. (c) and (d) Charging current density ($\Delta j = (j_+ - j_-)/2$) at −0.25 V vs. RHE plotted against the scan rate for $CaCu_3Ir_4O_{12}$ and IrO_2. The slope of the fitting line is used for determination of the double-layer capacitance (C_{dl}).

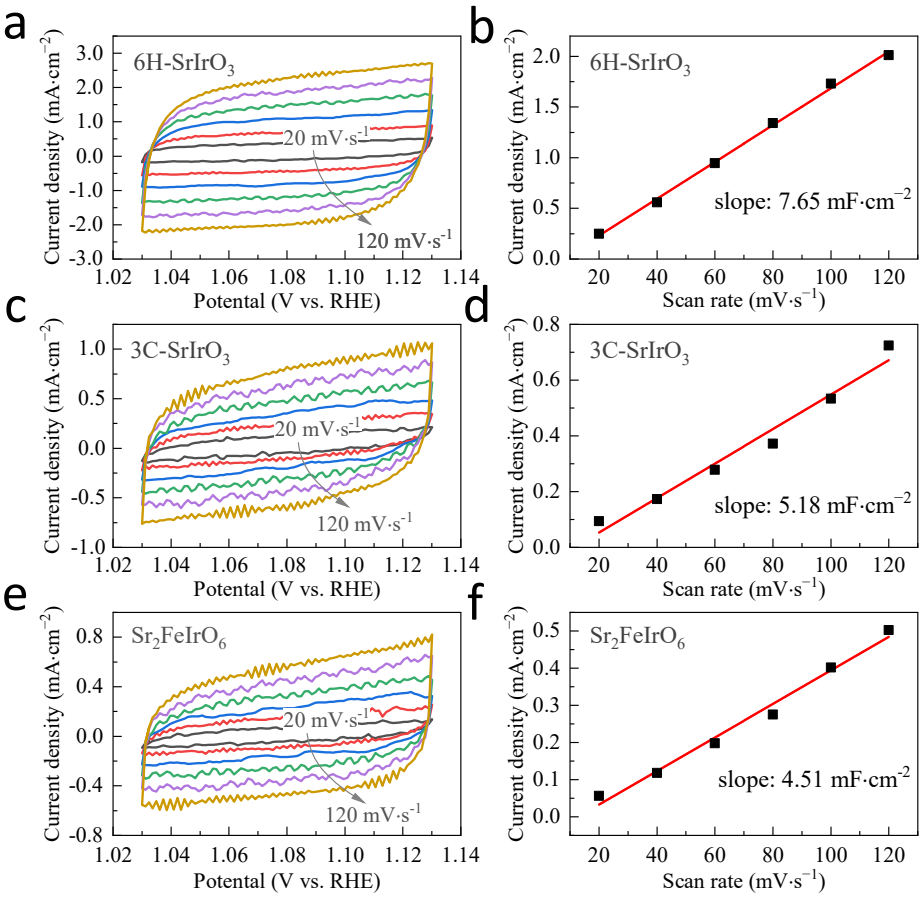

Figure S5. ECSA analyses of 6H-$SrIrO_3$, 3C-$SrIrO_3$ and Sr_2FeIrO_6 catalysts. (a), (c) and (e) Cyclic voltammograms at different scan rates in a potential window for 6H-$SrIrO_3$, 3C-$SrIrO_3$ and Sr_2FeIrO_6, respectively. (b), (d) and (f) Charging current density ($\Delta j = (j_+ - j_-)/2$) at −0.25 V vs. RHE plotted against the scan rate for 6H-$SrIrO_3$, 3C-$SrIrO_3$ and Sr_2FeIrO_6, respectively. The slope of the fitting line is used for determination of the double-layer capacitance (C_{dl}).

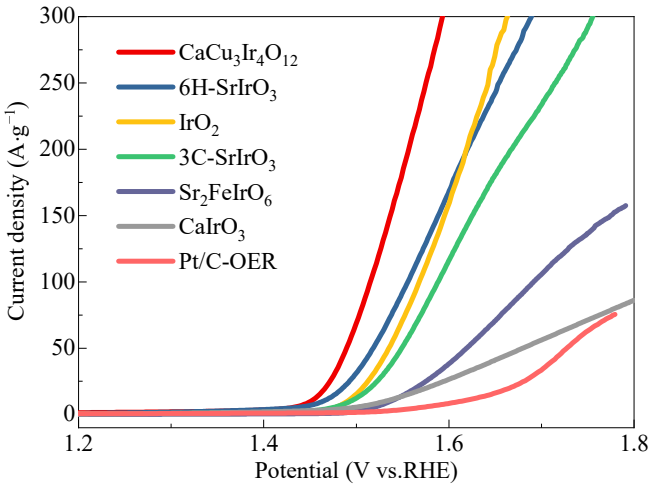

Figure S6. Mass activity based on the oxide weight at different potentials.

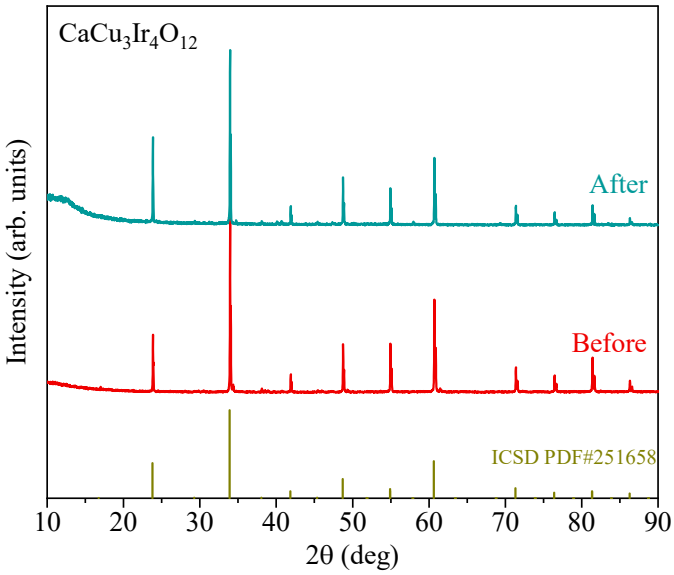

Figure S7. XRD patterns of $CaCu_3Ir_4O_{12}$ before and after OER with the standard pattern of ICSD PDF#251658.

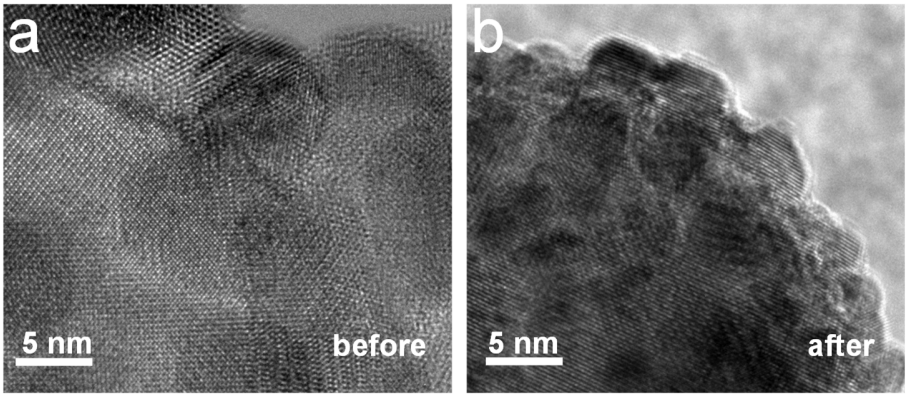

Figure S8. HRTEM images of $CaCu_3Ir_4O_{12}$ before (a) and after (b) OER.

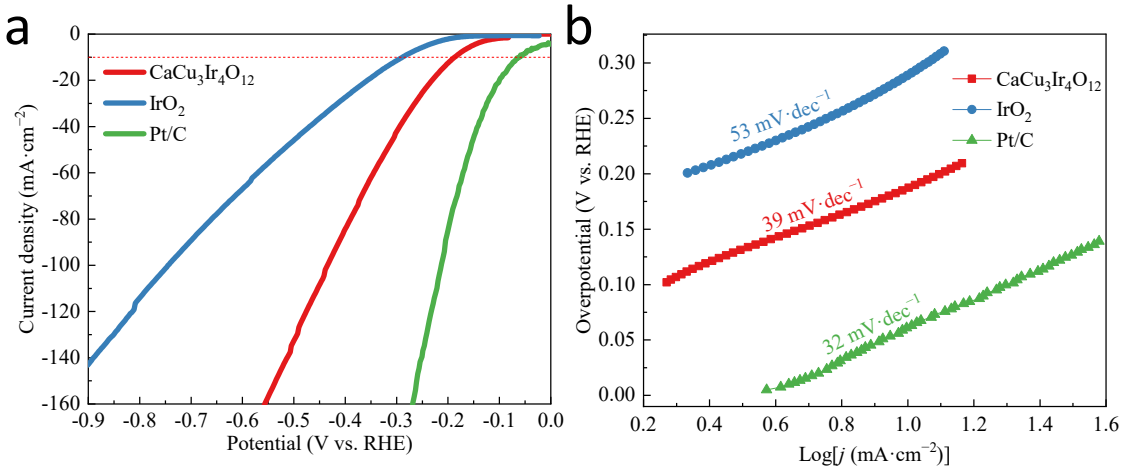

Figure S9. HER polarization curves of $CaCu_3Ir_4O_{12}$ and related references. (a) HER polarization curves in 1 -M KOH. (b) Corresponding Tafel plots derived from (a).

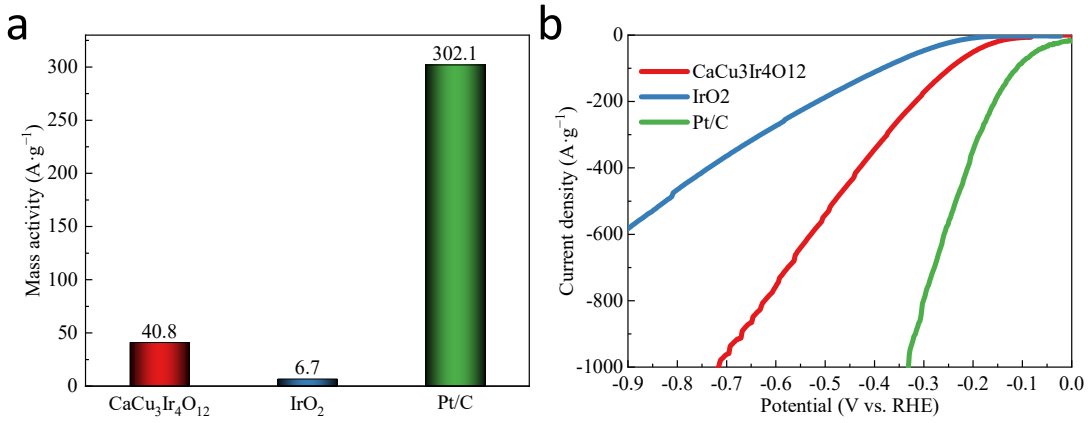

Figure S10. Mass activity for the HER. (a) Mass activities of the samples at the overpotential of 0.18 V vs. RHE. (b) Mass activity based on the oxide weight at different potentials.

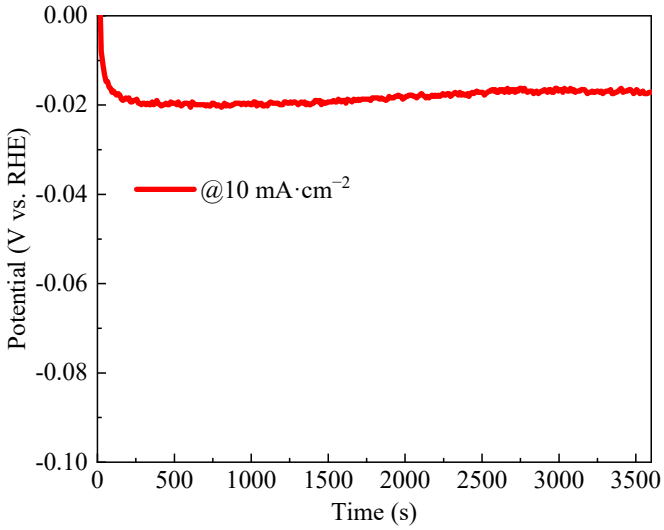

Figure S11. Chronopotentiometry measurement under the HER condition of $CaCu_3Ir_4O_{12}$ at 10 mA·cm^{-2}.

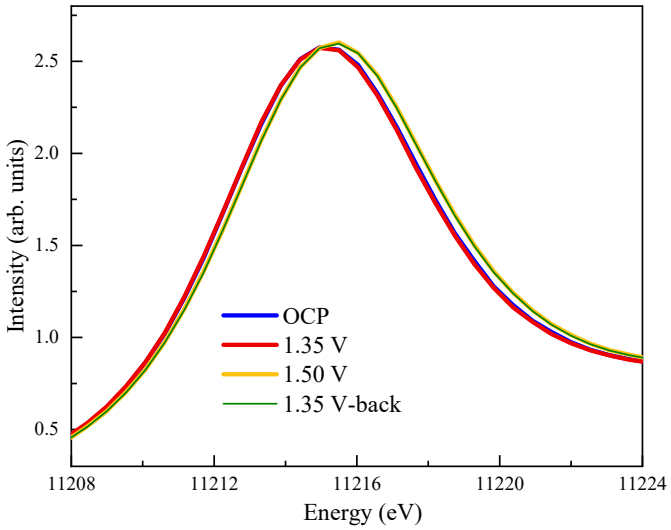

Figure S12. Normalized operando Ir L_3-edge XANES spectra with various potentials in 1 M KOH at ambient conditions. When the voltage is lowered to 1.35 V in the later stage of the reaction, the peak position is the same as that when the high voltage 1.50 V is applied, which indicates the irreversibility of the reaction.

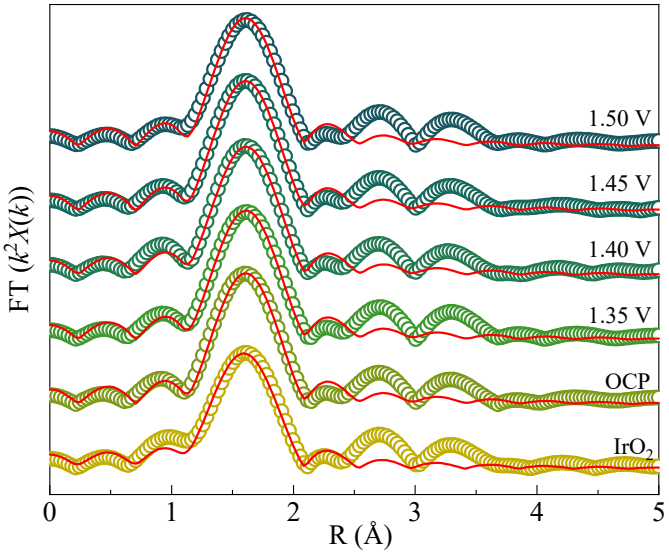

Figure S13. Fourier transformed k^2-weighted Ir L_3-edge EXAFS spectra of $CaCu_3Ir_4O_{12}$ with reference IrO_2 under various potentials. Hollow circles are FT-EXAFS spectra and red lines are fitted results. The peaks at 1.0–2.0 Å corresponds to the distance of Ir–O bond.

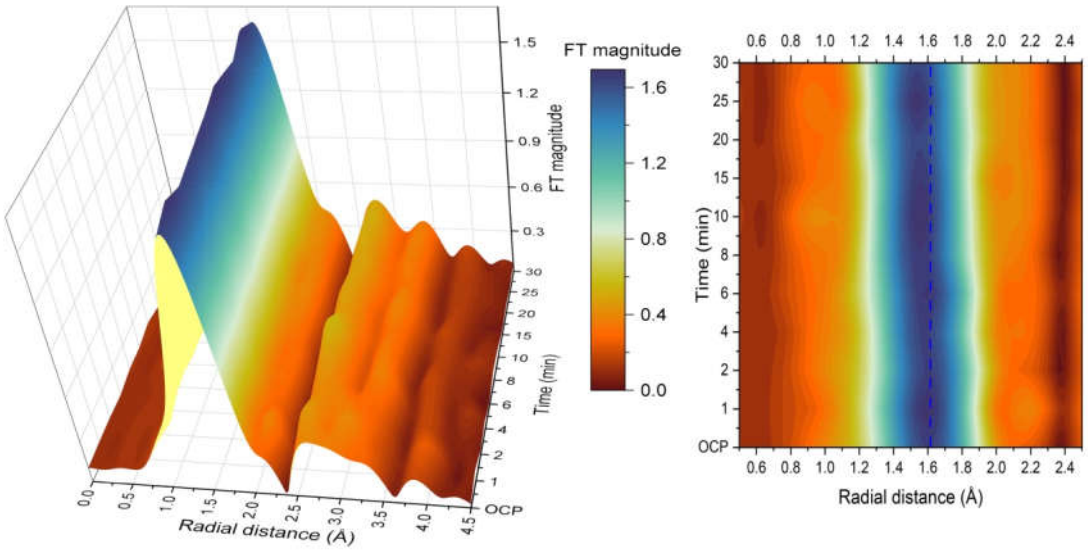

Figure S14. 3D and color map showing the time-dependent operando k^2-weighted FT-EXAFS spectra at Ir L_3-edge of $CaCu_3Ir_4O_{12}$.

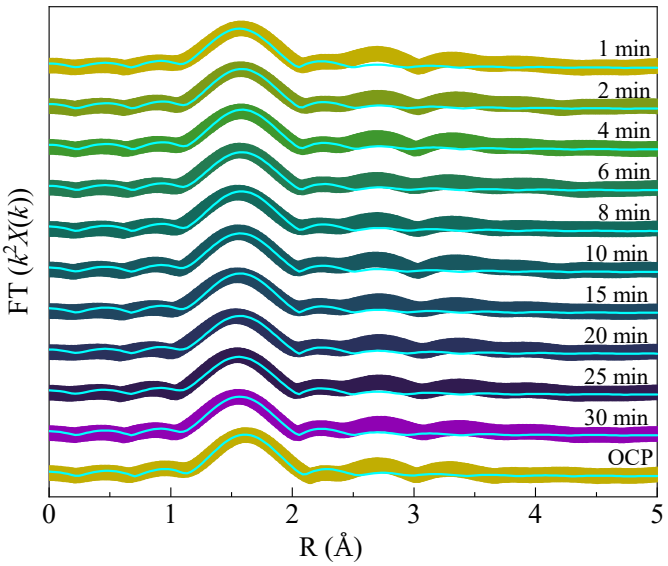

Figure S15. Fourier transformed k^2-weighted Ir L_3-edge EXAFS spectra of $CaCu_3Ir_4O_{12}$ with various time. Solid circles are the FT-EXAFS spectrum and cyan lines are fitted results. The peaks at 1.0–2.0 Å corresponds to the distance of Ir–O bond.

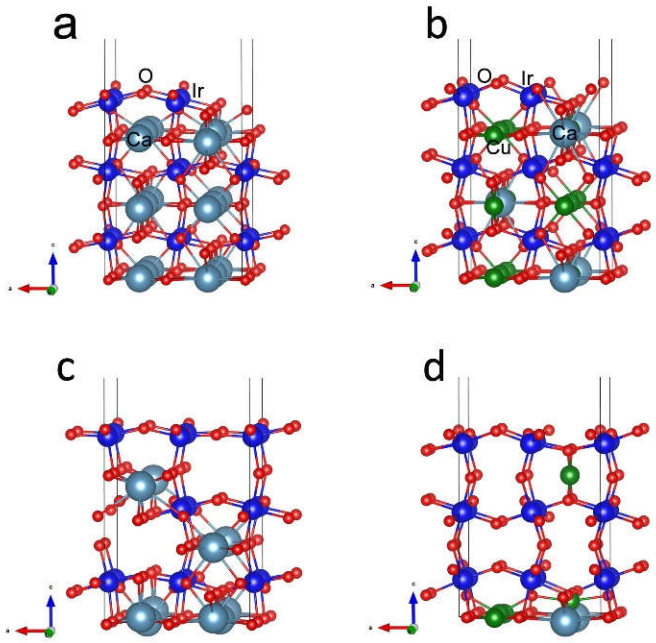

Figure S16. The optimized local structures for the (001) surface. (a) $CaIr^{4+}O_3$, (b) $CaCu_3Ir^{4+}{}_4O_{12}$, (c) $Ca_{0.5}Ir^{5+}O_3$, and (d) $Ca_{0.5}Cu_{1.5}Ir^{5+}{}_4O_{12}$. The blue-grey, blue, dark green, and red balls represent Ca, Ir, Cu, and O atoms, respectively.

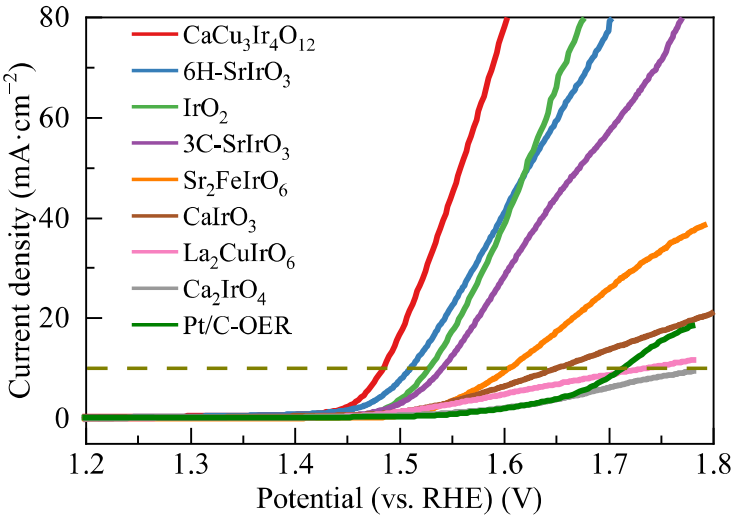

Figure S17. Systematic comparison of OER polarization curves for $CaCu_3Ir_4O_{12}$ and related references.

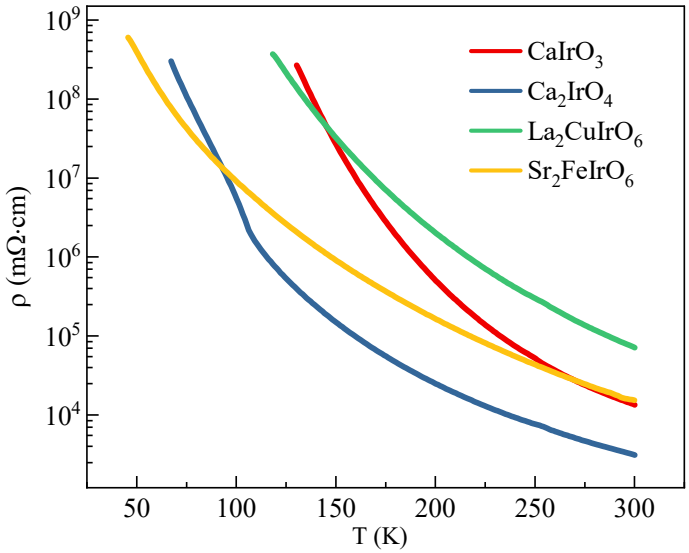

Figure S18. Temperature-dependent resistivity measured between 2–300 K for related insulating references.

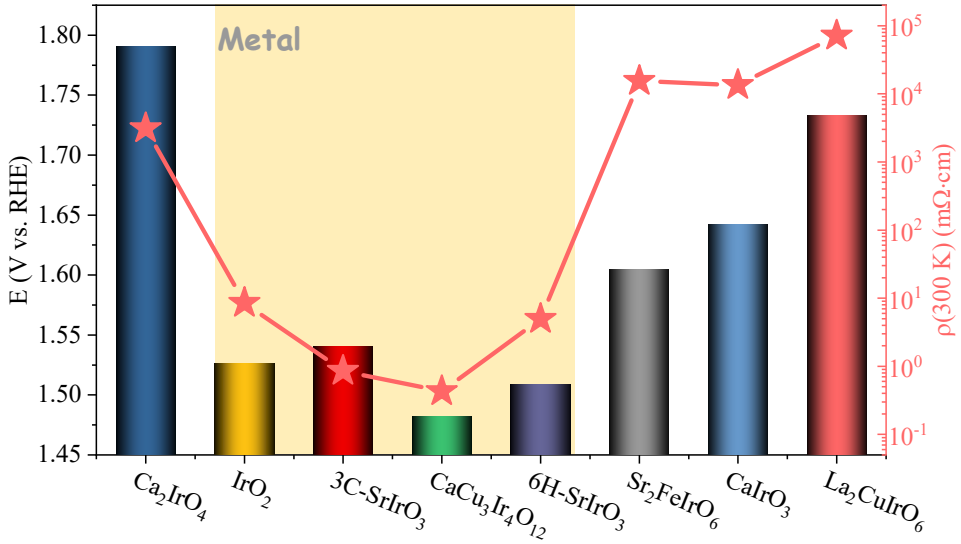

Figure S19. Systematic comparison of catalytic activity and conductivity for $CaCu_3Ir_4O_{12}$ and related references.

References

1. Xu, X.; Chen, Y.; Zhou, W.; Zhu, Z.; Su, C.; Liu, M.; Shao, Z., A Perovskite Electrocatalyst for Efficient Hydrogen Evolution Reaction. *Adv. Mater.* **2016,** *28* (30), 6442-6448.

2. Hua, B.; Li, M.; Pang, W.; Tang, W.; Zhao, S.; Jin, Z.; Zeng, Y.; Amirkhiz, B. S.; Luo, J.-L., Activating p-Blocking Centers in Perovskite for Efficient Water Splitting. *Chem* **2018,** *4* (12), 2902-2916.

3. Zhu, Y. L.; Zhou, W.; Zhong, Y. J.; Bu, Y. F.; Chen, X. Y.; Zhong, Q.; Liu, M. L.; Shao, Z. P., A Perovskite Nanorod as Bifunctional Electrocatalyst for Overall Water Splitting. *Adv. Energy Mater.* **2017,** *7* (8), No. 1602122.

4. Hua, B.; Li, M.; Zhang, Y.-Q.; Sun, Y.-F.; Luo, J.-L., All-In-One Perovskite Catalyst: Smart Controls of Architecture and Composition toward Enhanced Oxygen/Hydrogen Evolution Reactions. *Adv. Energy Mater.* **2017,** *7* (20), No. 1700666.

5. Dai, J.; Zhu, Y.; Zhong, Y.; Miao, J.; Lin, B.; Zhou, W.; Shao, Z., Enabling High and Stable Electrocatalytic Activity of Iron-Based Perovskite Oxides for Water Splitting by Combined Bulk Doping and Morphology Designing. *Adv. Mater. Interfaces* **2019,** *6* (1), No. 1801317.

6. Chen, G.; Hu, Z.; Zhu, Y.; Gu, B.; Zhong, Y.; Lin, H.-J.; Chen, C.-T.; Zhou, W.; Shao, Z., A Universal Strategy to Design Superior Water-Splitting Electrocatalysts Based on Fast In Situ Reconstruction of Amorphous Nanofilm Precursors. *Adv. Mater.* **2018,** *30* (43), No. 1804333.

7. Zhang, Z.; Chen, Y.; Dai, Z.; Tan, S.; Chen, D., Promoting hydrogen-evolution activity and stability of perovskite oxides via effectively lattice doping of molybdenum. *Electrochim. Acta* **2019,** *312*, 128-136.

8. Wang, C.; Zeng, L.; Guo, W.; Gong, C.; Yang, J., Enhancing oxygen and hydrogen evolution activities of perovskite oxide LaCoO3 via effective doping of platinum. *RSC Adv.* **2019,** *9* (61), 35646-35654.

9. Guan, D.; Zhou, J.; Hu, Z.; Zhou, W.; Xu, X.; Zhong, Y.; Liu, B.; Chen, Y.; Xu, M.; Lin, H.-J.; Chen, C.-T.; Wang, J.-Q.; Shao, Z., Searching General Sufficient-and-Necessary Conditions for Ultrafast Hydrogen-Evolving Electrocatalysis. *Adv. Funct. Mater.* **2019,** *29* (20), No. 1900704.

10. Wang, J.; Gao, Y.; Chen, D.; Liu, J.; Zhang, Z.; Shao, Z.; Ciucci, F., Water Splitting with an Enhanced Bifunctional Double Perovskite. *ACS Catal.* **2018,** *8* (1), 364-371.

11. Sun, Q.; Dai, Z.; Zhang, Z.; Chen, Z.; Lin, H.; Gao, Y.; Chen, D., Double perovskite PrBaCo2O5.5: An efficient and stable electrocatalyst for hydrogen evolution reaction. *J. Power Sources* **2019,** *427*, 194-200.

12. Zhu, Y. L.; Tahini, H. A.; Hu, Z. W.; Dai, J.; Chen, Y. B.; Sun, H. N.; Zhou, W.; Liu, M. L.; Smith, S. C.; Wang, H. T.; Shao, Z. P., Unusual synergistic effect in layered Ruddlesden - Popper oxide enables ultrafast hydrogen evolution. *Nat. Commun.* **2019,** *10*, No. 149.